magnetochemistry

MDPI

Article

Comprehensively Understanding the Transformation of Paramagnetic Tetramer to Spin-Paired Dimer in an S = ½ Molecular Crystal

Yin Qian [1], Yan Gao [1], Lei Xu [1], Reinhard K. Kremer [2,*], Jin Zhang [1] and Xiao-Ming Ren [1,2,3,*]

[1] State Key Laboratory of Materials-Oriented Chemical Engineering and College of Chemistry and Molecular Engineering, Nanjing Tech University, Nanjing 211816, China; yinqian@njtech.edu.cn (Y.Q.); 202261105089@njtech.edu.cn (Y.G.); xl8686666@163.com (L.X.); Zhangjin@ecust.edu.cn (J.Z.)
[2] Max-Planck-Institute für Festkörperforschung, Heisenbergstrasse 1, 70569 Stuttgart, Germany
[3] State Key Laboratory of Coordination Chemistry, Nanjing University, Nanjing 210023, China
* Correspondence: rekre@fkf.mpg.de (R.K.K.); xmren@njtech.edu.cn (X.-M.R.)

Abstract: In this study, we comparatively analyzed the variable-temperature crystal structures for two isomorphous salts, [1-benzyl-4-aminopyridinium][M(mnt)$_2$] (M = Ni or Cu; mnt^{2-} = maleonitriledithiolate; labeled as **APy-Ni** or **APy-Cu**). Both salts crystallize in the triclinic *P*–1 space group at 296 K, comprising linear [M(mnt)$_2$]$^-$ (M = Ni or Cu) tetramers. A magnetostructural phase transition occurs at T_C~190 K in S = ½ **APy-Ni** at ambient pressure, with a conversion of paramagnetic tetramers into nonmagnetic spin-paired dimers. The discontinuous alteration of cell parameters at T_C signifies the characteristic of first-order phase transition in **APy-Ni**. No such transition appears in the nonmagnetic **APy-Cu** within the same temperature vicinity, demonstrating the magnetic interactions promoting the structural phase transition in **APy-Ni**, which is further reinforced through a comparison of the lattice formation energy between **APy-Ni** and **APy-Cu**. The phase transition may bear a resemblance to the mechanisms typically observed in spin-Peierls systems. We further explored the magnetic and phase transition properties of **APy-Ni** under varying pressures. Significantly, T_C shows a linear increase with rising pressure within the range of 0.003–0.88 GPa, with a rate of 90 K GPa^{-1}, manifesting that the applied pressure promotes the transition from tetramer to dimer.

Keywords: metal-bis-dithiolene salt; thermotropic phase transition; piezotropic phase transition; linear tetramer; spin-paired dimer

Academic Editor: Jinkui Tang

Received: 10 January 2025
Revised: 19 January 2025
Accepted: 21 January 2025
Published: 24 January 2025

Citation: Qian, Y.; Gao, Y.; Xu, L.; Kremer, R.K.; Zhang, J.; Ren, X.-M. Comprehensively Understanding the Transformation of Paramagnetic Tetramer to Spin-Paired Dimer in an S = ½ Molecular Crystal. *Magnetochemistry* **2025**, *11*, 8. https://doi.org/10.3390/magnetochemistry11020008

1. Introduction

A fascinating phenomenon, crystal-to-crystal phase transition, has been observed in numerous materials. Such transitions can be categorized into two main types based on structural changes, i.e., displacement-type [1–4] and order–disorder-type [5–9] phase transitions. The former pertains to the relative displacement of atoms or molecules/ions, while the latter involves the rotational motion of groups or molecules/ions within the lattice. Displacement-type phase transitions generally occur with the assistance of phonons. For instance, the Jahn–Teller effect can trigger a displacement-type phase transition in polyatomic molecules with degenerate electronic states [10]. Similarly, a Peierls/spin-Peierls transition can occur in a one-dimensional half-filled band structure/S = ½ magnetic chain system [11–14]. Moreover, a displacement-type phase transition can take place in a ferroelectric/antiferroelectric crystal [1–4]. The order–disorder-type phase transition is

typically characterized by the presence of one or more components comprising globular-shaped molecules or ions within the lattice. Such molecules or ions exhibit minimal rotational energy barriers and considerable rotational freedom [5–9].

In a prior study, we documented the salt [1-benzyl-4-aminopyridinium][Ni(mnt)$_2$] (**APy-Ni**). This salt comprises linear [Ni(mnt)$_2$]$^-$ tetramers at ambient conditions, where the anion bears S = ½ spin, and exhibits a magnetostructural phase transition at T_C~190 K. It adopts a paramagnetic tetramer configuration in the high-temperature phase (HTP) and transitions to a spin-paired dimer configuration in the low-temperature phase (LTP) [15]. To gain a comprehensive understanding of the origin of the phase transition in **APy-Ni**, we synthesized the nonmagnetic crystals of [1-benzyl-4-aminopyridinium][Cu(mnt)$_2$] (**APy-Cu**). Notably, not only is **APy-Cu** isomorphous to **APy-Ni** at room temperature, but these two salts also exhibit remarkably analogous cell parameters and packing manner. In this study, we conducted a comparative investigation into the temperature-dependent crystal structures and lattice formation energies of **APy-Ni** and **APy-Cu**. Additionally, we explored the pressure-dependent magnetic and phase transition behaviors of **APy-Ni**. Our results revealed that the T_C exhibits ultra-sensitivity to external pressure (below 0.003 GPa), and the magnetic couplings play a crucial role in promoting the magnetostructural phase transition in **APy-Ni** as well.

2. Materials and Methods

2.1. Preparation of [1-Benzyl-4-aminopyridinium][M(mnt)$_2$] (M = Ni or Cu)

The microcrystalline sample of [1-benzyl-4-aminopyridinium][Ni(mnt)$_2$] (mnt^{2-} = maleonitriledithiolate; labeled as **APy-Ni**) was prepared following the published procedure [15]. The isomorphous analog [1-benzyl-4-aminopyridinium][Cu(mnt)$_2$] (abbr. as **APy-Cu**) was synthesized using the process that is similar to that of **APy-Ni**, only replacing the reactant $NiCl_2{\cdot}6H_2O$ by $CuCl_2{\cdot}2H_2O$. The yields of both salts are more than 60% calculated on the reactant $NiCl_2{\cdot}6H_2O$ or $CuCl_2{\cdot}2H_2O$.

Microanalysis: Calc. for $C_{20}H_{13}N_6NiS_4$ (**APy-Ni**): C, 45.81; H, 2.50; N, 16.03%. Found: C, 45.66; H, 2.62; N, 15.99%.

Microanalysis: Calc. for $C_{20}H_{13}N_6CuS_4$ (**APy-Cu**): C, 45.40; H, 2.48; N, 15.88%. Found: C, 45.28; H, 2.52; N, 15.64%.

2.2. X-Ray Single Crystallography

Diffraction data of selected crystals of **APy-Ni** were obtained on a Stoe IPDS diffractometer with an image plate detector (Mo-Kα, Ag-Kα radiation). Sections and projections of the reciprocal space were calculated from the raw data using diffractometer software [16]. The crystal data and structure refinements for **APy-Ni** at 296 and 100 K are represented in Table S1. The single-crystal X-ray diffraction data of **APy-Cu** at 296 and 100 K were performed by using Graphite monochromated Mo-Kα (λ = 0.71073 Å) on a Bruker D8 QUEST Apex III CCD area detector diffractometer. Data reduction and absorption correction were performed with the SAINT [17] and SADABS [18] software packages, respectively. The crystal structures were solved by direct method and refined on F^2 using the full-matrix least-squares method with the SHELXTL package [19]. All hydrogen atoms were geometrically fixed and placed in an ideal position. The crystal data and structure refinements for **APy-Cu** at 296 and 100 K are summarized in Table S2.

The details of other instruments and methods used in this study are provided in Supplementary Materials.

3. Results and Discussion

3.1. Crystal Structures

The single-crystal X-ray diffraction data were acquired at 296 and 100 K for both **APy-Ni** and **APy-Cu**. The crystallographic details are summarized in Tables S1 and S2 and Table 1, and the packing diagrams are shown in Figures S2–S7. Both **APy-Ni** and **APy-Cu** are isomorphous at room temperature, exhibiting closely comparable cell parameters and packing arrangements. While maintaining a comparable packing mode, a structural phase transition was observed in **APy-Ni** around 190 K. Conversely, no corresponding phase transition was noted in **APy-Cu** within the same temperature vicinity (Figure S1b). As a result, the two salts display slightly distinct packing structures at 100 K.

Table 1. The typical crystallographic data for **APy-Ni** and **APy-Cu** at 296 and 100 K.

Salt	**APy-Ni**		**APy-Cu**	
Temp./K	296	100	296	100
Crystal system	Triclinic	Triclinic	Triclinic	Triclinic
Space group	*P*–1	*P*–1	*P*–1	*P*–1
a/Å	11.2264 (8)	11.322 (2)	11.2559 (5)	11.156 (4)
b/Å	14.2879 (10)	13.933 (3)	14.2885 (7)	14.099 (4)
c/Å	15.6204 (11)	15.458 (3)	15.5951 (8)	15.445 (5)
α/°	73.879 (6)	73.07 (3)	74.420 (5)	75.166 (10)
β/°	77.289 (6)	74.32 (3)	77.931 (4)	77.667 (10)
γ/°	67.915 (6)	67.63 (3)	68.227 (4)	67.527 (9)
V/Å^3	2211.5 (3)	2121.9 (7)	2226.8 (2)	2151.8 (12)

Given the analogous molecular and packing structures of **APy-Ni** and **APy-Cu**, we shall focus our comprehensive crystal structure elucidation solely on **APy-Ni**. In both the HTP and LTP, the crystal structure of **APy-Ni** is categorized within the triclinic *P*–1 space group, with nearly identical cell parameters. The asymmetric unit has two pairs of crystallographically independent anions and cations, illustrated in Figure 1a (where the hydrogen atoms are omitted for clarity). Differentiating anions and cations are distinguished as Ni1/Ni2 and N10/N12, respectively. Two distinct planar $[Ni(mnt)_2]^-$ anions show an approximate parallel alignment, with their mean molecular planes composed of Ni and four S atoms, forming a dihedral angle of 2.44° in HTP and 1.12° in LTP. The two different cations present a Λ-shaped configuration. Notably, the bond lengths and bond angles within both anions and cations are in excellent accordance with values previously reported in the literature [15].

As illustrated in Figures 1b and S2–S4, the cations are arranged in a wave-shaped layer, aligning parallel to the (010) crystallographic plane. Meanwhile, the $[Ni(mnt)_2]^-$ anions, situated within channels formed by adjacent cationic layers, form tetrameric stacks along the a-axis direction. Within each tetramer, neighboring anions adopt a parallel face-to-face arrangement, connected by intermolecular S. . .S interactions with adjacent anion tetramers. In addition to the electrostatic interactions between anions and cations, the structure reveals charge-assisted hydrogen bonds. These hydrogen bonds occur between the NH_2 groups in cations and the CN groups in mnt ligands, as well as between hydrogen atoms within phenyl/pyridyl rings and the CN groups of mnt ligands (Figures 2 and S8).

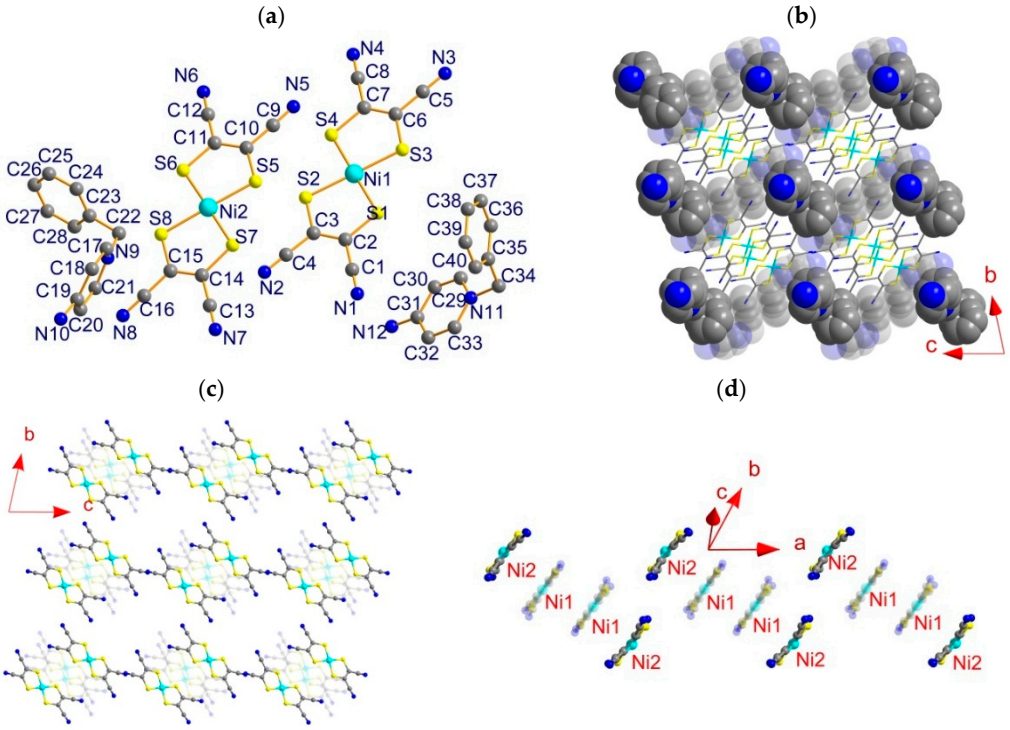

Figure 1. (**a**) An asymmetric unit (here, all hydrogen atoms omitted for clarity), (**b**) packing diagram viewed along a-axis wherein the cations with N10 and N12 are represented in the translucent and opaque modes, (**c**) arranging manner of anions viewed along a-axis wherein the anions with Ni1 and Ni2 are represented in the translucent and opaque modes, (**d**) tetrameric chain of anions along a-axis in **APy-Ni**.

For the sake of facilitating a comprehensive comparison between the crystal structure alterations of **APy-Ni** from its HTP to LTP, we have delineated pertinent distances. These include intermolecular Ni. . .Ni, Ni. . .S, and S. . .S distances, as well as the mean molecular plane of anions within a tetramer and the S. . .S distances between adjacent anion tetramers. These intermolecular contacts are visually highlighted in Figure 2a–c. The distances associated with charge-assisted hydrogen bonds between anions and cations, along with the shortest C. . .C distance between phenyl and pyridyl rings of neighboring cations, are depicted in Figure 2d,e. A summarized overview of these distances can be found in Tables 2 and 3. The phase transition results in discernible changes in the crystal structure, with the primary alterations involving the following aspects: (1) Within a tetramer, the distances concerning the closest neighboring Ni1. . .Ni2 separations (labeled as a1) and Ni1. . .Ni1 separations (labeled as a2) have undergone unequal reductions. This phenomenon arises due to the contraction of two Ni1 anions along the longer molecular axis of $[Ni(mnt)_2]^-$ anion (Figure 2f,g). (2) Concomitantly, the distances between the mean molecular planes of adjacent anions (designated as a7 and a8 in Figure 2b) have also experienced non-uniform reductions. This effect is due to the contraction of the tetramer along its stacking direction. The above-mentioned structural modifications are a direct consequence of the phase transition. The Δ = a2 − a1 value is 0.15 Å in the HTP versus 0.351 Å in the LTP, indicating that the terminal and central $[Ni(mnt)_2]^-$ anions in a tetramer are strongly dimerized in the LTP regarding that in the HTP. From the viewpoint of structural change, the phase transition of tetramer–dimer belongs to the displacement-type structural phase transition. The S. . .S contacts between inter-tetramers (a9–a12) decrease, suggesting that the adjacent tetramers get close from the HTP to the LTP. (3) With respect to those in the HTP, the N. . .H distances between NH_2 groups and CN groups (b5, b7, and b9) are decreased and others expended, and the shortest C. . .C distance between phenyl and pyridyl rings of neighboring cations is increased in the LTP.

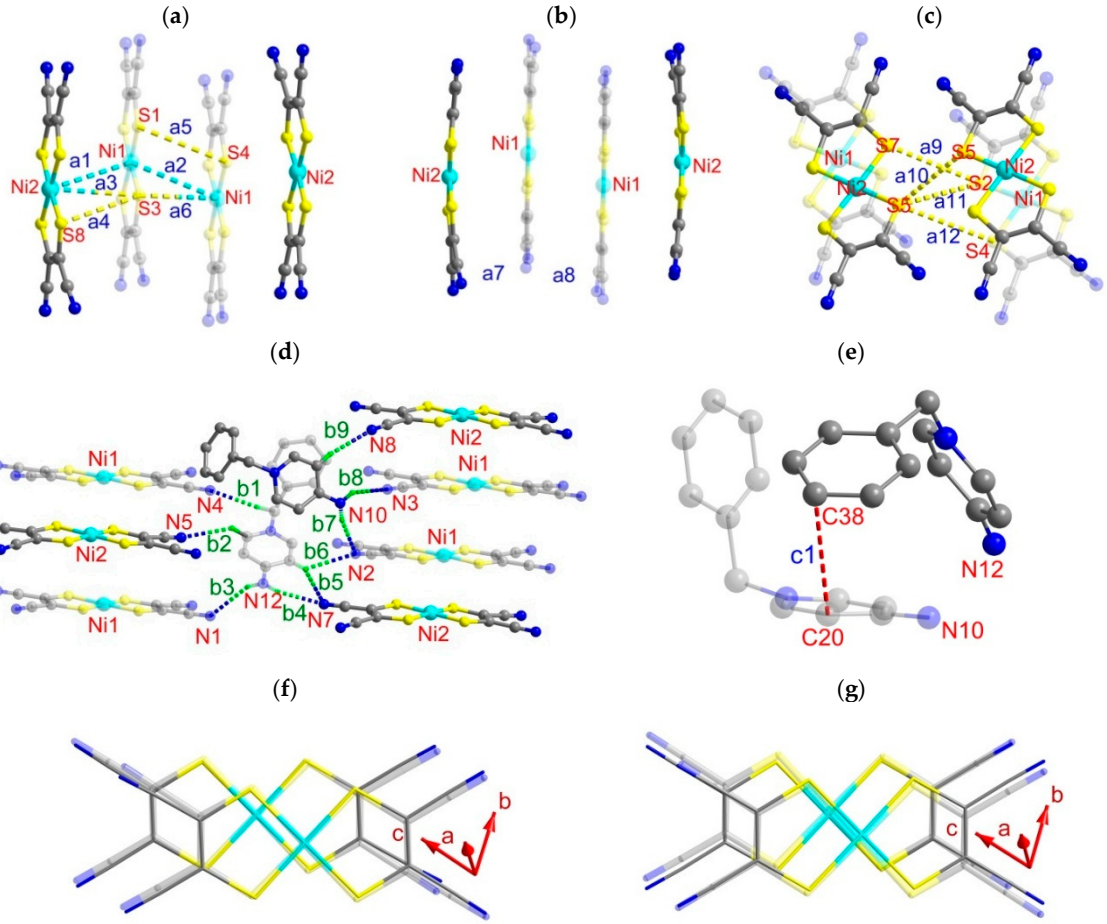

Figure 2. Schematic illustration of (**a**) typical intermolecular Ni. . .Ni, Ni. . .S, and S. . .S distances in an anion tetramer, (**b**) the separation of mean molecule plane between neighboring anions in an anion tetramer, (**c**) the S. . .S contacts between adjacent anion tetramers, (**d**) the charge-assisted H-bonds between adjacent anions and cations, (**e**) the shortest C. . .C distance between phenyl and pyridyl rings of neighboring cations, and top view of an anion tetramer in (**f**) HTP and (**g**) LTP in **APy-Ni**.

Table 2. The typical intermolecular distances (Å) within an anion tetramer of **APy-Ni** and **APy-Cu** at 296 and 100 K.

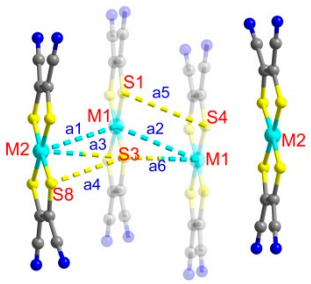

Distance/Å	APy-Ni		APy-Cu	
	296 K	**100 K**	**296 K**	**100 K**
a1	3.953	3.897	4.004	3.947
a2	3.944	3.546	3.984	3.919
a3	3.815	3.801	3.906	3.950
a4	3.867	3.519	3.998	3.953
a5	3.991	3.972	4.098	4.095
a6	3.585	3.549	3.506	3.368

Table 3. The typical intermolecular distances between anions and between anion and cation as well as between cations in both HTP (296 K) and LTP (100 K) of **APy-Ni**.

Distance/Å	296 K	100 K	Distance/Å	296 K	100 K
a7	3.561	3.455	b6	2.692	2.541
a8	3.517	3.542	b7	2.171	2.252
a9	3.886	3.841	b8	2.436	2.289
a10	3.891	3.721	b9	2.691	3.116
a11	3.591	3.589	c1	3.376	3.441

*3.2. Temperature-Dependent Cell Parameters and PXRD Patterns of **APy-Ni***

The temperature-dependent cell parameters of **APy-Ni** were assessed through single-crystal X-ray diffraction analysis. The variation in relative cell parameters [$P_{cell}(T)/P_{cell}(293\ K)$] vs. T is presented in Figures 3a and S9, revealing significant anisotropic tendencies. In the HTP, the a-axis and the α angle demonstrate a distinct negative thermal expansion behavior. Conversely, the remaining unit cell parameters decrease as the temperature decreases. Around 190 K, it is noteworthy that all cell parameters undergo a sudden discontinuous alteration, exhibiting the characteristic of the first-order phase transition. In the LTP, the c-axis exhibits negative thermal expansion behavior, while the other cell parameters display positive thermal expansion tendencies.

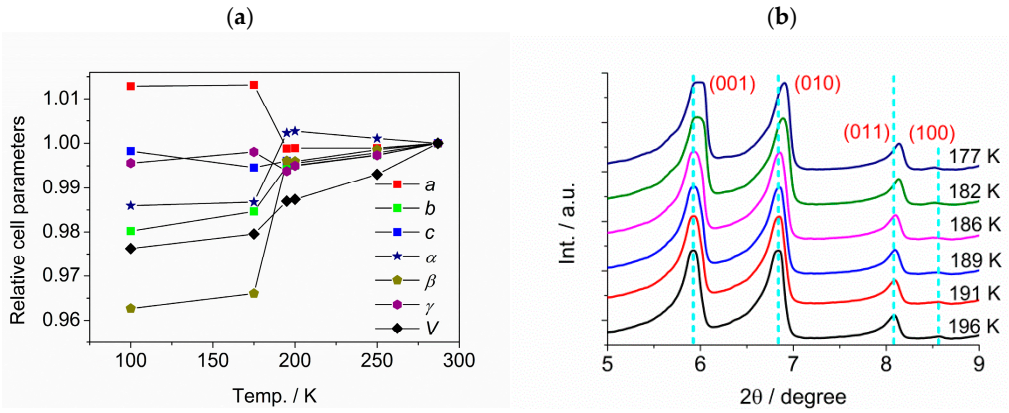

Figure 3. (**a**) Temperature-dependent unit cell parameters; (**b**) variable-temperature powder X-ray patterns around phase transition for **APy-Ni**.

The varying temperature PXRD patterns of **APy-Ni** are illustrated in Figures 3b and S9a,b. These patterns show remarkable similarity within the temperature range of 164–286 K. Transitioning from HTP to LTP, subtle distinctions in the PXRD patterns become apparent. Remarkably, the (001), (010), and (011) diffraction peaks shift toward the higher angle side, while the (100) diffraction peak shifts toward the lower angle side. This observation is consistent with the expansion of the a-axis and the contraction of both b- and c-axes, as shown in Figure 3a. Furthermore, the observable changes appear in the diffraction peaks at $2\theta \approx 9.2$ and 11.9°, which shift toward the lower and higher angle sides, respectively. The relative intensities of double diffraction peaks, such as those at $2\theta \approx 13.5$ and 13.7° as well as 15.6 and 16.0°, exhibit a contrasting trend of alteration (Figure S10b). These notable observations indicated the presence of two-phase equilibria within a temperature range of approximately ±10 K around the critical temperature (T_C). This is evidenced by the superposition of PXRD patterns in the LTP and HTP regions during this temperature interval.

3.3. Magnetic Properties at Ambient Pressure and DSC Features

The plot of χ_m vs. T is depicted in Figure 4a for **APy-Ni**; herein, the molar magnetic susceptibility, χ_m, corresponds to one $[Ni(mnt)_2]^-$ anion per formula. On the basis of the crystal structure analyses in both LTP and HTP, the magnetic behaviors of **APy-Ni** may be described by an S = ½ AFM dimer in the LTP and a linear S = ½ tetramer in the HTP, respectively [20]. An isolated dimer involving two S = ½ centers, which are coupled by a magnetic exchange constant J in line with the spin Hamiltonian $\hat{H} = -2\hat{S}_1 \cdot \hat{S}_2$ [20] the temperature dependences of magnetic susceptibility follow the Bleaney–Bowers expression, i.e., the first term in Equation (1) [21]. In consideration of the Curie–Weiss-type paramagnetism manifested within the low-temperature regime, it becomes essential to address the magnetic impurities associated with this phenomenon. These impurities, often arising from lattice defects, stem from structural imperfections that result in the presence of uncoupled monomers. Additionally, the diamagnetism observed in closed shells and the potential occurrence of van Vleck paramagnetism probably contribute to the whole experimental magnetic susceptibility; therefore, the whole experimental χ_m(T) of **APy-Ni** may be written as the form in Equation (1) in the LTP:

$$\chi_m = \frac{Ng^2\mu_B^2}{k_B T} \cdot \frac{1}{\left[3 + \exp\left(-\frac{2J}{k_B T}\right)\right]} + \frac{C}{T} + \chi_0 \quad (1)$$

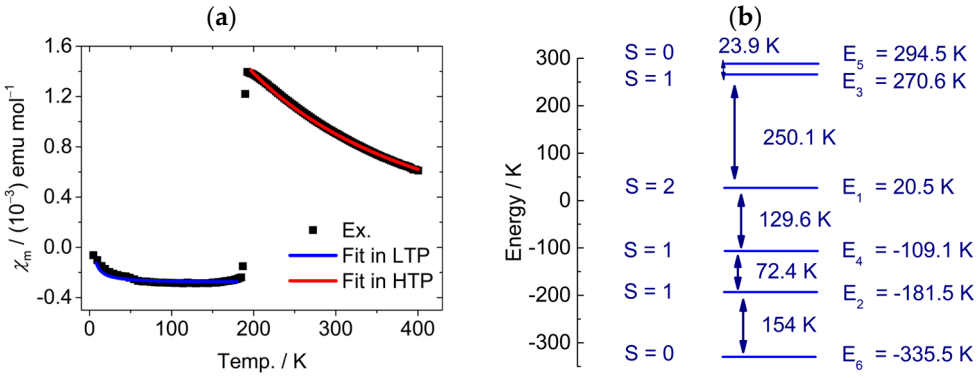

Figure 4. (**a**) Plot of χ_m vs. T in the temperature range of 5–400 K on heating (the solid squares and red/blue lines represent the experimental data and fits, respectively); (**b**) the low-lying state energy level diagram for a linear S = ½ tetramer (J_1/k_B = −101 K and J_2/k_B = 161 K) in the HTP for **APy-Ni**.

The best fit produced the parameters of $J/k_B \approx -320$ K, $C = 2.9 \times 10^{-3}$ emu K mol^{-1} and $\chi_0 = -3.17 \times 10^{-4}$ emu mol^{-1} with g = 2.015 (fixed) [20], which is quite close to the average of g-factor value 2.017 obtained from variable-temperature EPR spectra analyses (ref. next section). The amount of magnetic impurity is estimated to be ca. 0.8% based on the fitted Curie constant. The χ_0 value is comparable to the Pascal's constants of **APy-Ni**. The spin gap ($\Delta_{spin}/k_B = 2J/k_B$) in LTP is quantified at ~640 K, and so a big spin gap resulted in **APy-Ni** exhibiting almost diamagnetism at much higher temperature (~180 K; see Figures 4a and 5b). The whole experimental $\chi_m(T)$ of **APy-Ni** in HTP includes three parts, shown in Equations (2)–(4), in which the first term represents the contribution from a linear S = ½ tetramer spin system with two different magnetic exchange constants within a spin-tetramer based on the spin Hamiltonian $\hat{H} = -2J_1(\hat{S}_1 \cdot \hat{S}_2 + \hat{S}_3 \cdot \hat{S}_4) - 2J_2\hat{S}_2 \cdot \hat{S}_3$ [20,22], the J_1 and J_2 correspond to the magnetic exchange constant between the terminal and the neighboring central spins as well as the magnetic exchange constant between two central spins, and the last two terms have the same meanings as those in Equation (1). The best fit for the χ_m–T plot of **APy-Ni** in the HTP (190–400 K) using the Equations (2)–(4) [22]

offered $J_1/k_B \approx -101$ K and $J_2/k_B \approx 161$ K with C and χ_0 fixed to the same values in the LTP. The results obtained from fits suggest that the terminal and central anions feature AFM coupling, while two central anions exhibit FM exchange interactions within an anion tetramer. As illustrated in Figure 4a, both the experimental and the fitted χ_m–T profiles match well with each other, demonstrating that the magnetic coupling model and the fitted results seem reasonable. On the basis of the E_i (i = 1–6) values, the spin energy gap between the singlet ground state (E_6 with S = 0) and the first magnetic excited state (E_1 with S = 1) is ~154 K, and the low-lying state energy level diagram is displayed in Figure 4b.

$$\chi_m = \frac{Ng^2\mu_B^2}{k_B T}\cdot\frac{A}{Z} + \frac{C}{T} + \chi_0 \quad (2)$$

$$A = 10\exp\left(-\frac{E_1}{k_B T}\right) + 2\exp\left(-\frac{E_2}{k_B T}\right) + 2\exp\left(-\frac{E_3}{k_B T}\right) + 2\exp\left(-\frac{E_4}{k_B T}\right) \quad (3)$$

$$Z = 5\exp\left(-\frac{E_1}{k_B T}\right) + 3[\exp\left(-\frac{E_2}{k_B T}\right) + \exp\left(-\frac{E_3}{k_B T}\right) + \exp\left(-\frac{E_4}{k_B T}\right) + \exp\left(-\frac{E_5}{k_B T}\right) + \exp\left(-\frac{E_6}{k_B T}\right)] \quad (4)$$

$$E_1 = -J_1 - \frac{1}{2}J_2 \ (S = 2)$$

$$E_2 = J_1 - \frac{1}{2}J_2 \ (S = 1)$$

$$E_3 = \frac{1}{2}J_2 + \left(J_1^2 + J_2^2\right)^{1/2} \ (S = 1)$$

$$E_4 = \frac{1}{2}J_2 - \left(J_1^2 + J_2^2\right)^{1/2} \ (S = 1)$$

$$E_5 = J_1 + \frac{1}{2}J_2 + \left(4J_1^2 - 2J_1J_2 + J_2^2\right)^{1/2} \ (S = 0)$$

$$E_6 = J_1 + \frac{1}{2}J_2 - \left(4J_1^2 - 2J_1J_2 + J_2^2\right)^{1/2} \ (S = 0)$$

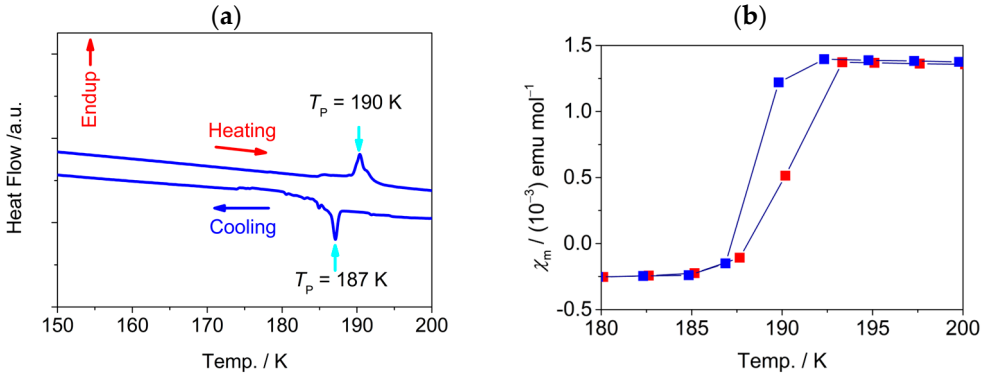

Figure 5. (**a**) DSC plots of **APy-Ni** in the heating–cooling cycle and (**b**) temperature-dependent magnetic susceptibility of **APy-Ni** showing a small hysteresis loop close to the phase transition.

The DSC traces obtained at a heating/cooling rate of 1 K min^{-1} are depicted in Figure 5a. These traces reveal distinct exothermic and endothermic anomalies occurring at ~187 K during cooling and ~190 K during heating, respectively. The noticeable thermal hysteresis observed in both DSC and χ_m vs. T plots (Figure 5) between these temperatures strongly indicates the presence of the first-order phase transition characteristics. This inference finds further support in the abrupt alteration of lattice parameters around the critical temperature (T_C). The enthalpy change (ΔH) associated with the phase transition is quantified at 1.52 kJ mol^{-1}, while

an entropy difference (ΔS) of 8.04 J mol^{-1} K^{-1} is determined during heating [15]. In general, the ΔS associated with a phase transition includes the contributions from structure (molecular orientations) entropy changes, vibrational entropy changes, and magnetic entropy changes for a magnetic insulator. The crystal structure analyses for **APy-Ni** revealed analogous packing structures in both the HTP and the LTP. This implies that the entropy change (ΔS) of the phase transition primarily arises from the alterations in spin states. As discussed in the part of magnetic property analysis, **APy-Ni** displays paramagnetism, characterized by the presence of a linear S = ½ tetramer in the HTP, while diamagnetism in the LTP owing to the formation of spin-paired dimers composed of S = ½ $[Ni(mnt)_2]^-$ anions, the spin entropy change (ΔS) corresponding to the magnetostructural phase transition is calculated as $\Delta S = R\ln(Z_{HTP}/Z_{LTP})$, with R (=8.314 J mol^{-1} K^{-1}) denoting the gas constant and Z_{HTP}, Z_{LTP} representing the partition functions in the HTP and the LTP sequentially, which are expressed in the form of Equations (5) and (6) correspondingly.

$$Z_{HTP} = 1 + 3\exp\left(-\frac{E_2 - E_6}{k_B T}\right) + 3\exp\left(-\frac{E_4 - E_6}{k_B T}\right) + 5\exp\left(-\frac{E_1 - E_6}{k_B T}\right) + 3\exp\left(-\frac{E_3 - E_6}{k_B T}\right) + \exp\left(-\frac{E_5 - E_6}{k_B T}\right) \quad (5)$$

$$Z_{LTP} = \left[1 + 3\exp\left(-\frac{\Delta}{k_B T}\right)\right]^2 \quad (6)$$

In Equation (5), E_i (i = 1–6) denotes the spin energy levels (Figure 4b) in the HTP. In Equation (6), Δ signifies the spin energy gap between the singlet ground state and the triplet excited state in the LTP. The squared term arises from the transformation of a spin-tetramer in the HTP into two spin-dimers in the LTP. Taking T_C as 190 K, the values of E_i (i = 1 to 6) in the HTP and Δ in the LTP were determined through the fits of variable-temperature magnetic susceptibilities. Subsequently, the spin entropy change (ΔS) was computed to be ~10.24 J mol^{-1} K^{-1}. This result, slightly bigger than the ΔS value of 8.04 J mol^{-1} K^{-1} determined by DSC measurements, provides further support for the conclusion that the observed ΔS at T_C primarily originates from modifications in the spin states.

*3.4. EPR Spectra of **APy-Ni** in the Temperature of 110–292 K*

Figure S11 displays EPR spectra of **APy-Ni** in 110–292 K. Above 170 K, **APy-Ni** exhibits isotropic broad Lorentzian-shaped signals, which can be well fit by taking the field derivative of both the '+' and '−' absorption signal into consideration. The fits revealed a typical line width of ~1500 Oe, the g-factors about 1% larger than the free electron value, and the averaged g-factor amounts to 2.017 in 170–292 K (Figure S11b), indicating small orbital contributions to the magnetic moment, and this conclusion is consistent with the theoretic analysis, i.e., the singly occupied molecular orbital (SOMO) in the $[Ni(mnt)_2]^-$ anion with D_{2h} point group symmetry is comprised of the d_{x2-y2} orbital of Ni and the group orbitals of $[(mnt)_2]^{4-}$ ligands with a_g symmetry [23], and the spin population on the Ni atom was calculated to be only ~0.21 [24]. As shown in Figure 6a, the EPR spectrum of **APy-Ni** displays the superposition of two signals at 160 K, namely, an isotropic broad signal arising from tetramers together with a narrow and asymmetric signal, as well as only narrow and asymmetric signal below 160 K, and its intensity is enhanced upon cooling (Figure 6b). The inset in Figure 6a shows that the χ_m value decays exponentially in 110–190 K and tends to be unchanged below 160 K, demonstrating that, below 160 K, no magnetic excited state is populated in the thermal equilibrium distribution of a magnetic tetramer. Thus, the narrow and asymmetric resonance signals originate from the uncoupled magnetic impurities, which arise from the defect of the lattice.

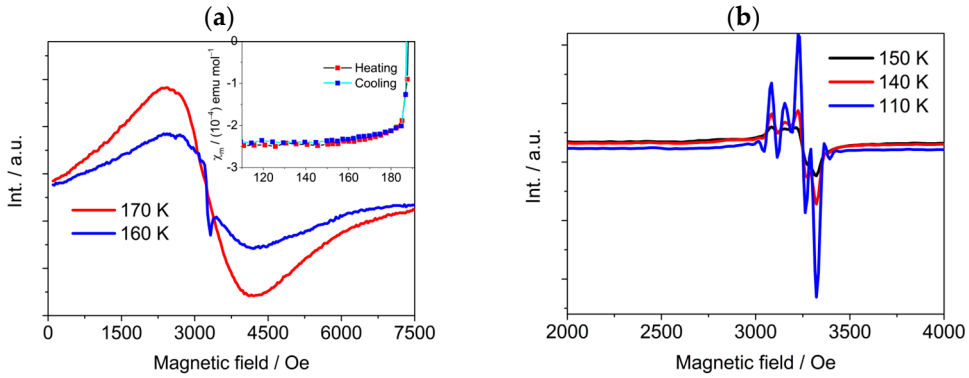

Figure 6. EPR spectra of a powdered polycrystalline sample of **APy-Ni** at (**a**) 160 and 170 K (inset: χ_m–T plots in 110–190 K) and (**b**) 110, 140, and 150 K.

*3.5. Phase Transition Behavior of **APy-Ni** Under Pressures*

With respect to inorganic matters, molecular crystals display greater compressibility and, as a result, exhibit higher sensitivity for pressure detection, and this is verified by some examples, e.g., a Cu^{2+} complex with nitroxide [Cu(hfac)$_2$NN-PzMe] shows a spin crossover-like phenomenon with $T_C \approx 150$ K at ambient pressure, which significantly shifts from 150 to 300 K as the hydrostatic pressure increases from 10^{-4} to 0.14 GPa [25]. Two salts, [R-BzPy][Ni(mnt)$_2$] (R-BzPy$^+$ = 1-(4′-nitrobenzyl)pyridinium with R = NO_2 and 1-(4′-brominobenzyl)pyridinium with R = Br), show spin-Peierls transition at $T_{SP} \approx 184$ and 112 K under ambient pressure, respectively, and T_{SP} rises at an average rate of 1.66 K GPa^{-1} for R = NO_2 and 0.82 K GPa^{-1} for R = Br [26].

From a theoretical standpoint, the Clausius–Clapeyron relation elucidates the connection between pressure (P) and the critical temperature (T_C) of a phase transition within the equilibrium of two phases. This is expressed as follows:

$$\frac{dP}{dT} = \frac{\Delta H}{T_C \Delta V} \tag{7}$$

where P and T represent pressure and temperature, respectively. T_C denotes the critical temperature of the phase transition, while ΔH and ΔV refer to the alterations in enthalpy and volume associated with the phase transition at T_C. This equation can be rewritten as follows:

$$lnT_c = \frac{\Delta V}{\Delta H} P + C \tag{8}$$

where C is a constant. From the LTP to the HTP, **APy-Ni** shows positive expansion in cell volume and endothermal behavior, indicative of the T_C of tetramer–dimer transformation increasing with increasing pressure.

The pressure behavior of the phase transition was further studied by measuring the temperature dependences of magnetic susceptibility at different applied pressures and under the magnetic field of 1.0×10^4 Oe (Supplementary Materials). The T_C was determined reliably from the peak temperature of the quantity $d(\chi_m T)/dT$ (Figure 7a), which increases with an increase in pressure. In a narrow pressure regime (from ambient to 0.003 GPa), the T_C sharply jumps. Subsequently, the T_C almost linearly increases with a rate of 90 K GPa^{-1} from 0.003 to 0.88 GPa (Figures 7b and S12). Obviously, this slope in the plot of T_C vs. P is much less than in the initially applied pressure stage because the Coulomb repulsion between ions increases rapidly as the pressure is elevated, resulting in the compressibility of the crystalline sample decreases. To the best of our knowledge, the averaged $\Delta T_C/\Delta P$ value of **APy-Ni** in the pressure range of 0.003–0.88 GPa is the largest one in the reported molecule-based spin transition compounds [27]. The T_C in **APy-Ni** is

remarkably sensitive to pressure, especially under initial lower pressure, demonstrating that the magnetic couplings between adjacent $[Ni(mnt)_2]^-$ anions are highly sensitive to the intermolecular arrangement [28]; moreover, the applied pressure promotes the transformation of tetrameric phase to dimeric phase. It is worth noting that the sample recovered from 0.88 GPa to ambient pressure shows the same T_C as the pristine sample, indicating that the transformation under pressure is reversible for **APy-Ni**. Materials that display a reversible piezotropic phase transition and demonstrate a linear correlation between applied pressure and critical temperature hold the capability to convert mechanical stimuli into various outputs, including optical [29,30], electrical [31,32], or magnetic signals [25,26,33,34]. These materials can be employed for real-time monitoring of pressure fluctuations, offering potential applications in fields such as unsteady flow field measurement [35,36] and artificial intelligence development [37,38].

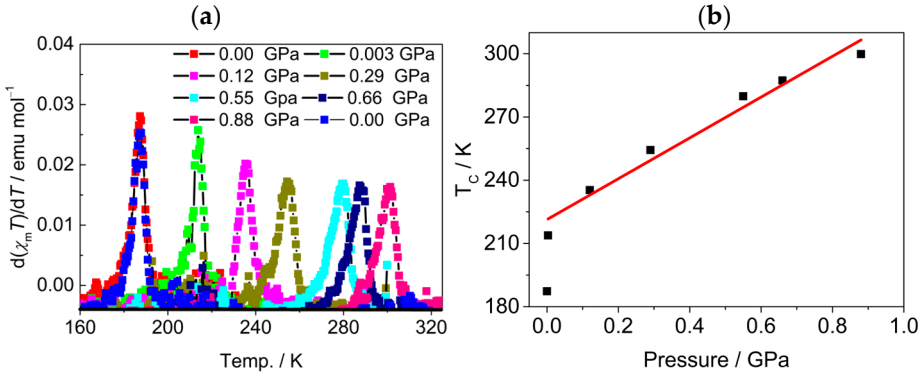

Figure 7. (**a**) Plots of $d(\chi_m T)/dT$ vs. T at different external pressures and (**b**) pressure dependence of T_C for **APy-Ni**.

*3.6. The Formation Energy of Lattice of **APy-Ni** and **APy-Cu***

The formation energy of lattice ($\Delta E_{lattice}$) per molar unit cell was defined as the difference between the cumulative energy of the constituent components (E_{anion} and E_{cation}) and the total energy of the crystal ($E_{crystal}$) per molar unit cell and calculated utilizing the Density Functional Theory (DFT) method via the Dmol^3 program [39–41]. In the crystal structures of isomorphous **APy-Ni** and **APy-Cu**, both at 296 K and 100 K, four pairs of anions and cations exist. The computed values of $\Delta E_{lattice}$, $E_{crystal}$, E_{anion}, and E_{cation} for these crystal structures (**APy-Ni** and **APy-Cu**) at both 296 K and 100 K are summarized in Table 4. The findings indicate that, at both 296 K and 100 K, **APy-Ni** exhibits higher formation energy of lattice compared to **APy-Cu**. This discrepancy is attributed to the magnetic interactions among anions present in the paramagnetic **APy-Ni**, which confer supplementary stability energy for its lattice formation when contrasted with the nonmagnetic **APy-Cu**. As the temperature decreases, lattice contraction leads to a notable elevation in the formation energy of lattice for both **APy-Ni** and **APy-Cu**. Specifically, upon cooling from 296 to 100 K, the formation energy of the lattice increased by 51.98 kJ mol^{-1} for **APy-Ni** and 7.35 kJ mol^{-1} for **APy-Cu**. This difference is noticeable, with the former increase being substantially larger than the latter.

Table 4. The calculated $\Delta E_{lattice}$, $E_{crystal}$, E_{anion}, and E_{cation} for **APy-Ni** and **APy-Cu** at 296 and 100 K.

	* E_{anion}/Hartree	* E_{cation}/Hartree	$E_{crystal}$/Hartree	$\Delta E_{lattice}$/Hartree	$\Delta E_{lattice}$/kJ mol^{-1}
APy-Cu (100 K)	−3756.1185	−573.886	−17,320.9663	0.9483	2489.76
APy-Cu (296 K)	−3756.1185	−573.886	−17,320.9635	0.9455	2482.41
APy-Ni (100 K)	−3623.9881	−573.886	−16,792.4758	0.9794	2571.41
APy-Ni (296 K)	−3623.9881	−573.886	−16,792.456	0.9596	2519.43

* E_{anion} and E_{cation} represent the energy of per anion and per cation, respectively.

Both **APy-Cu** and **APy-Ni** are classified as ionic crystals, with their $\Delta E_{lattice}$ primarily arising from Coulomb interactions, specifically Madelung energy. The $\Delta E_{lattice}$ values of **APy-Cu** exhibit a slight increase at 100 K compared to 296 K, attributed to lattice contraction at lower temperatures, leading to an enhancement of Coulomb interactions. In the case of **APy-Ni**, magnetic exchange interactions contribute significantly, in addition to Coulomb interactions. This divergence can be linked to the notably stronger magnetic interactions present in the LTP compared to the HTP for **APy-Ni**. These findings unveil the pivotal role of magnetic interactions in the transformation from a paramagnetic tetramer to a spin-paired dimer within **APy-Ni**.

It is well known that the electron– or spin–vibronic couplings (so-called electron– or spin–phonon interactions) play a crucial role in the phase transition that occurs in one-dimensional half-filled electron band structure or S = ½ spin systems, e.g., the conventional Peierls or spin-Peierls transition systems [11–14]. It is likely that the magnetoelastic interactions contribute to this displacement-type of tetramer–dimer transition, bearing a resemblance to the mechanisms typically observed in spin-Peierls systems.

4. Conclusions

In this study, we have investigated the crystal structures and magnetic properties of an S = ½ linear tetramer salt (**APy-Ni**). **APy-Ni** exhibits a magnetostructural phase transition with a T_C around 190 K at ambient pressure and adopts a paramagnetic tetramer configuration in the HTP, whereas a diamagnetic dimer configuration in the LTP. Investigation into the pressure-dependent magnetic behaviors has unveiled the remarkable response of T_C to varying pressures attributed to the substantial compressibility of van der Waals crystals. A strong linear correlation between T_C and pressure (P) has been observed within the pressure range of 0.003–0.88 GPa, with an average rate of change ($\Delta T_C/\Delta P$) of ~90 K GPa^{-1}, demonstrating the applied pressure promoting the spin transition by compressing the lattice, which enhances the magnetic couplings within the tetramer. The sensitivity of T_C to applied pressure also suggests that **APy-Ni** holds potential as a material for pressure-sensing applications. The isomorphous nonmagnetic salt (**APy-Cu**) shares similar cell parameters and packing arrangements with **APy-Ni** at ambient conditions. Nevertheless, the absence of the tetramer–dimer transformation within the same temperature range implies a pronounced influence of magnetic interactions on the structural phase transition of **APy-Ni**, resembling the spin-Peierls transition observed in S = ½ linear chain systems. This hypothesis is supported by the calculated lattice formation energy. Overall, these findings provide a foundation for the development of novel molecule-based smart materials that demonstrate sensitivity to pressure variations, particularly within moderate pressure ranges.

Supplementary Materials: The following supporting information can be downloaded at https://www.mdpi.com/article/10.3390/magnetochemistry11020008/s1, Table S1: Crystal data for **APy-Ni**, Table S2: Crystal data for **APy-Cu** at 296 and 100 K. Figure S1: (a) Experimental and simulated PXRD patterns of **APy-Cu**, and (b) DSC plot of **APy-Cu.** Figure S2: Packing diagrams of **APy-Ni** viewed

along *b*- and *c*-axes, respectively. Figure S3: Packing diagrams in both ball–stick and space-filling modes of cations in *APy-Ni* viewed along *a*-, *b*-, and *c*-axes. The cations with N10 and N12 are represented in translucent and opaque modes, respectively. Figure S4: (a) Top and (b) side views of a cationic layer in **APy-Ni**. The cations with N10 and N12 are represented in translucent and opaque modes, respectively. Figure S5: ORTEP plots of **APy-Cu** at (a) 296 K and (b) 100 K, all of which the thermal ellipsoid was drawn at the 30% probability level. Figure S6: Packing diagrams of **APy-Cu** at 296 K viewed along *a*-axis direction, which showed (a) the tetramers of anions residual in the channels enclosed by cations and (b) the arrangement of anions. Figure S7: Packing diagrams of anions in the crystal structure of **APy-Cu** at 296 K, showing the arranging manner between neighboring tetramers. Figure S8: The Hirshfeld surfaces of APy-Ni for visualizing intermolecular interactions between cations and anions (a–c) in HTP (296 K) and (d–f) in LTP (100 K). The cation contains N10 in (a,d), as well as N12 in (b,c,e,f), in which the red dots represent the H-bonding interactions between H atoms of the −NH2 group or phenyl ring/pyridyl ring and the −CN groups of mnt^{2-} in the anions. Obviously, the number of red dots increases in LTP compared to that in HTP owing to contraction of cell volume. Figure S9: Variable-temperature cell parameters with error bars of **APy-Ni**. Figure S10: (a,b) Variable-temperature powder X-ray patterns of **APy-Ni**. Figure S11: (a–e) Plots of the EPR signals measured for a powder sample of **APy-Ni** at 9.3 GHz at different temperatures in 110–292 K, and (f) plots of line width *versus* T and g-factor *versus* T in 160−292 K. Figure S12: Plot of TC versus applied pressure with error bars for **APy-Ni**. See refs. [39,41–50].

Author Contributions: Y.Q., Y.G. and L.X.: synthesized the samples, performed the power and part of single-crystal X-ray experiments, and data analysis; Y.Q.: performed Harshifeld surface analysis; J.Z.: performed the calculations for overlap integrals and lattice formation energy; R.K.K.: performed collection and analysis of temperature-dependent EPR spectra; R.K.K. and X.-M.R.: supervised the study and revised the manuscript. All authors have read and agreed to the published version of the manuscript.

Funding: This research was funded by the National Natural Science Foundation of China, grant number 22073047. XMR acknowledges the Max-Planck Society for financial support.

Data Availability Statement: All data generated and analyzed during this study are included in the article and its Supplementary Information. The crystal structures generated in this study have been deposited in the Cambridge Crystallographic Data Centre under accession code CCDC: 2177252, 2177253, 2291616, and 2291618, and can be obtained free of charge from the CCDC via https://www.ccdc.cam.ac.uk/structures/ (accessed on 9 January 2025).

Acknowledgments: The authors thank E. Brücher for the magnetic property determinations, G. Siegle for DSC analyses, and W. Röthenbach for variable-temperature X-ray powder diffraction measurements.

Conflicts of Interest: The authors declare no conflicts of interest.

Abbreviations

The following abbreviations are used in this manuscript:

APy-Ni	[1-benzyl-4-aminopyridinium][$Ni(mnt)_2$]
APy-Cu	[1-benzyl-4-aminopyridinium][$Cu(mnt)_2$]
APy^+	1-benzyl-4-aminopyridinium
mnt^{2-}	Maleonitriledithiolate
AFM	Antiferromagnetic
FM	Ferromagnetic

References

1. Maksimov, E.G. Theoretical Investigations of the Ferroelectric Transition. *Physics−Uspekhi* **2009**, *52*, 603–614. [CrossRef]
2. Nakano, A.; Hasegawa, T.; Tamura, S.; Katayama, N.; Tsutsui, S.; Sawa, H. Antiferroelectric Distortion with Anomalous Phonon Softening in the Excitonic Insulator Ta_2NiSe_5. *Phys. Rev. B* **2018**, *98*, 045139. [CrossRef]

3. Luo, Y.; Zhang, Y.Q.; Xu, G.C. Synthesis and Characterization of a Displacement-Type Ferroelectric–Ferroelectric Phase Transition Compound $[(NH_3)(CH_2)_3(NH_3)]_2[InBr_6]Br{\cdot}H_2O$. *Inorg. Chem.* **2022**, *61*, 13143–13148. [CrossRef] [PubMed]
4. Morosov, A.I.; Sigov, A.S. The Nature of Central Peak in $SrTiO_3$. *Ferroelectrics* **2011**, *412*, 12–14. [CrossRef]
5. Harada, J.; Shimojo, T.; Oyamaguchi, H.; Hasegawa, H.; Takahashi, Y.; Satomi, K.; Suzuki, Y.; Kawamata, J.; Inabe, T. Directionally Tunable and Mechanically Deformable Ferroelectric Crystals from Rotating Polar Globular Ionic Molecules. *Nat. Chem.* **2016**, *8*, 946–952. [CrossRef]
6. Liu, H.Y.; Zhang, H.Y.; Chen, X.G.; Xiong, R.G. Molecular Design Principles for Ferroelectrics: Ferroelectrochemistry. *J. Am. Chem. Soc.* **2020**, *142*, 15205–15218. [CrossRef]
7. Xu, K.; Zhou, Z.N.; Han, X.B.; Yang, Y.W.; Zhang, W.; Ye, Q. Shape Shifting and Locking in Mechanically Responsive Organic-Inorganic Hybrid Materials for Thermoelastic Actuators. *Angew. Chem. Int. Ed.* **2024**, *63*, e202408247. [CrossRef]
8. Zhou, Q.J.; He, L.; Xu, K.; Han, X.B.; Yin, T.J.; Zhang, W.; Ye, Q. Thermally Reversible Luminescence in Ferroelastic Phase Transition Materials. *Adv. Opt. Mater.* **2024**, *12*, 2302292. [CrossRef]
9. Gui, L.A.; Chen, J.; Zhang, Y.F.; Li, L.H.; Li, J.R.; Hu, Z.B.; Zhang, S.Y.; Zhang, J.; Zhang, Z.; Ye, H.Y.; et al. Room-temperature Magnetocapacitance Spanning 97 K Hysteresis in Molecular Material. *Angew. Chem. Int. Ed.* **2024**, e202416380. [CrossRef]
10. Jahn, H.A.; Teller, E. Stability of Polyatomic Molecules in Degenerate Electronic States—I: Orbital Degeneracy. *Proc. R. Soc. Lond. A* **1937**, *161*, 220–235.
11. Peierls, R.E. *Quantum Theory of Solids*; Oxford University Press: London, UK, 1955; pp. 108–114.
12. Bray, J.W.; Hart, H.R., Jr.; Interrante, L.V.; Jacobs, I.S.; Kasper, J.S.; Watkins, G.D.; Wee, S.H.; Bonner, J.C. Observation of a Spin-Peierls Transition in a Heisenberg Antiferromagnetic Linear-Chain System. *Phys. Rev. Lett.* **1975**, *35*, 744–747. [CrossRef]
13. Braden, M.; Hennion, B.; Reichardt, W.; Dhalenne, G.; Revcolevschi, A. Spin-Phonon Coupling in $CuGeO_3$. *Phys. Rev. Lett.* **1998**, *80*, 3634–3637. [CrossRef]
14. Musfeldt, J.L.; Wang, Y.J.; Jandl, S.; Poirier, M.; Revcolevschi, A.; Dhalenne, G. Infrared Investigation of the Broken-Symmetry Ground State in $GeCuO_3$. *Phys. Rev. B* **1996**, *54*, 469–473. [CrossRef] [PubMed]
15. Ren, X.M.; Meng, Q.J.; Song, Y.; Hu, C.J.; Lu, C.S.; Chen, X.Y.; Xue, Z.L. Unusual Magnetic Property Associated with Dimerization within a Nickel Tetramer. *Inorg. Chem.* **2002**, *41*, 5931–5933. [CrossRef]
16. *Stoe IPDS Software Package Version 2.89*; Stoe & Cie. GmbH: Darmstadt, Germany, 1989.
17. Bruker. *APEX 2, SAINT, XPREP*; Bruker AXS Inc.: Madison, WI, USA, 2007.
18. Bruker. *SADABS*; Bruker AXS Inc.: Madison, WI, USA, 2001.
19. Sheldrick, G.M. A Short History of SHELX. *Acta Crystallogr. Sect. A Found. Crystallogr.* **2008**, *64*, 112–122. [CrossRef]
20. Ren, X.M.; Kremera, R.K.; Meng, Q.J. Investigation of the Magneto-Structural Phase Transition in [1-benzyl-4-aminopyridinium][bis(maleonitriledithiolato)-nickelate]. *J. Mag. Mag. Mater.* **2004**, *272–276*, 924–926. [CrossRef]
21. Carlin, R.L. *Magnetochemistry*; Springer: Berlin/Heidelberg, Germany, 1986; Chapter 5.
22. Rubenacker, G.V.; Drumheller, J.E.; Emerson, K.; Willett, R.D. Magnetic Susceptibility of $((CH_3)_3NH)_2Cu_4Br_{10}$, Chains of Stacked Linear Tetramers. *J. Mag. Mag. Mater.* **1986**, *54–57*, 1483–1484. [CrossRef]
23. Shupack, S.I.; Billig, E.; Clark, R.J.H.; Willams, R.; Gray, H.B. The Electronic Structures of Square-Planar Metal Complexes. V. Spectral Properties of the Maleonitriledithiolate Complexes of Nickel, Palladium, and Platinum. *J. Am. Chem. Soc.* **1964**, *86*, 4594–4602. [CrossRef]
24. Ni, Z.; Ren, X.; Ma, J.; Xie, J.; Ni, C.; Chen, Z.; Meng, Q. Theoretical Studies on the Magnetic Switching Controlled by Stacking Patterns of Bis(maleonitriledithiolato)nickelate(III) Dimers. *J. Am. Chem. Soc.* **2005**, *127*, 14330–14338. [CrossRef]
25. Maryunina, K.Y.; Zhang, X.; Nishihara, S.; Inoue, K.; Morozov, V.A.; Romanenko, G.V.; Ovcharenko, V.I. A Heterospin Pressure Sensor. *J. Mater. Chem. C* **2015**, *3*, 7788–7791. [CrossRef]
26. Ren, X.M.; Nishihara, S.; Akutagawa, T.; Fujita, W.; Awaga, K. Pressure Effect on Spin-Peierls-Like Transition in Quasi-1D Spin Systems [RBzPy][Ni(mnt)$_2$]. *Chem. Phys. Lett.* **2007**, *439*, 318–322. [CrossRef]
27. Tanaka, T.; Fujita, W.; Awaga, K. Pressure Effects on Magnetic Bistability in a Heterocyclic Thiazyl Radical TTTA. *Chem. Phys. Lett.* **2004**, *393*, 150–152. [CrossRef]
28. Coomber, A.T.; Beljonne, D.; Friend, R.H.; Brédas, J.L.; Charlton, A.; Robertson, N.; Underhill, A.E.; Kurmoo, M.; Day, P. Intermolecular Interactions in the Molecular Ferromagnetic $NH_4Ni(mnt)_2{\cdot}\ H_2O$. *Nature* **1996**, *380*, 144. [CrossRef]
29. Bao, H.; Wang, W.; Li, X.; Liu, X.; Zhang, L.; Yan, X.; Wang, Y.; Wang, C.; Jia, X.; Sun, P.; et al. Interfacial Stress-Modulated Mechanosensitive Upconversion Luminescence of $NaErF_4$ Based Heteroepitaxial Core–Shell Nanoparticles. *Adv. Opt. Mater.* **2022**, *10*, 2101702. [CrossRef]
30. Matsuda, Y.; Orimo, R.; Abe, Y.; Hiraiwa, Y.; Okamura, Y.; Sunami, Y. Pressure-Sensitive Nano-Sheet for Optical Pressure Measurement. *Sensors* **2021**, *21*, 7168. [CrossRef]
31. Chen, Z.; Zhuo, H.; Hu, Y.; Lai, H.; Liu, L.; Zhong, L.; Peng, X. Wood-Derived Lightweight and Elastic Carbon Aerogel for Pressure Sensing and Energy Storage. *Adv. Funct. Mater.* **2020**, *30*, 1910292. [CrossRef]

32. Zhao, S.; Ran, W.; Wang, D.; Yin, R.; Yan, Y.; Jiang, K.; Lou, Z.; Shen, G. 3D Dielectric Layer Enabled Highly Sensitive Capacitive Pressure Sensors for Wearable Electronics. *ACS Appl. Mater. Interfaces* **2020**, *12*, 32023–32030. [CrossRef]
33. Codjovi, E.; Menendez, N.; Jeftic, J.; Varret, F. Pressure and Temperature Hysteresis in the Spin-Transition Solid $Fe(btr)_2(NCS)_2 \cdot H_2O$, Pure and Diluted in Ni Matrix. *Acad. Sci. Ser. IIC Chem.* **2001**, *4*, 181–188.
34. Linares, J.; Codjovi, E.; Garcia, Y. Pressure and Temperature Spin Crossover Sensors with Optical Detection. *Sensors* **2012**, *12*, 4479–4492. [CrossRef]
35. Gregory, J.W.; Sakaue, H.; Liu, T.; Sullivan, J.P. Fast Pressure-Sensitive Paint for Flow and Acoustic Diagnostics. *Annu. Rev. Fluid Mech.* **2014**, *46*, 303–330. [CrossRef]
36. Peng, D.; Liu, Y. Fast Pressure-Sensitive Paint for Understanding Complex Flows: From Regular to Harsh Environments. *Exp. Fluids* **2020**, *61*, 8. [CrossRef]
37. Zhang, D.; Xu, S.; Zhao, X.; Qian, W.; Bowen, C.R.; Yang, Y. Wireless Monitoring of Small Strains in Intelligent Robots via a Joule Heating Effect in Stretchable Graphene–Polymer Nanocomposites. *Adv. Funct. Mater.* **2020**, *30*, 1910809. [CrossRef]
38. Persano, L.; Dagdeviren, C.; Su, Y.; Zhang, Y.; Girardo, S.; Pisignano, D.; Huang, Y.; Rogers, J.A. High Performance Piezoelectric Devices Based on Aligned Arrays of Nanofibers of Poly(vinylidenefluoride-co-trifluoroethylene). *Nat. Commun.* **2013**, *4*, 1633. [CrossRef]
39. Delley, B. From Molecules to Solids with the $DMol^3$ Approach. *J. Chem. Phys.* **2000**, *113*, 7756–7764. [CrossRef]
40. Perdew, J.P.; Burke, K.; Ernzerhof, M. Generalized Gradient Approximation Made Simple. *Phys. Rev. Lett.* **1996**, *77*, 3865–3868. [CrossRef]
41. Monkhorst, H.J.; Pack, J.D. Special Points for Brillouin-zone Integrations. *Phys. Rev. B* **1976**, *13*, 5188–5192. [CrossRef]
42. Simon, A. Eine Methode zur Untersuchung extrem luftempfindlicher Substanzen mit der Guinier-Methode. *J. Appl. Crystallogr.* **1970**, *3*, 11. [CrossRef]
43. Kremer, R.K.; Loa, I.; Razavi, F.S.; Syassen, K. Effect of pressure on the magnetic phase transition in α'-NaV_2O_5. *Solid State Commun.* **2000**, *113*, 217. [CrossRef]
44. Frisch, M.J.; Trucks, G.W.; Schlegel, H.B.; Scuseria, G.E.; Robb, M.A.; Cheeseman, J.R. *GAUSSIAN 09*; Revision A.02; Gaussian Inc.: Wallingford, CT, USA, 2009.
45. Lu, T.; Chen, F. Multiwfn: A multifunctional wavefunction analyzer. *J. Comput. Chem.* **2012**, *33*, 580–592. [CrossRef]
46. Becke, A.D. Density-functional thermochemistry. I. The effect of the exchange-only gradient correction. *J. Chem. Phys.* **1993**, *98*, 5648–5652. [CrossRef]
47. Lee, C.; Yang, W.; Parr, R.G. Development of the Colle-Salvetti correlation-energy formula into a functional of the electron density. *Phys. Rev. B* **1988**, *37*, 785–789. [CrossRef] [PubMed]
48. Delley, B. Hardness conserving semilocal pseudopotentials. *Phys. Rev. B* **2002**, *66*, 155125. [CrossRef]
49. Delley, B. An all-electron numerical method for solving the local density functional for polyatomic molecules. *J. Chem. Phys.* **1990**, *92*, 508–517. [CrossRef]
50. Tkatchenko, A.; Scheffler, M. Accurate Molecular Van Der Waals Interactions from Ground-State Electron Density and Free-Atom Reference Data. *Phys. Rev. Lett.* **2009**, *102*, 073005. [CrossRef] [PubMed]